ENGINEERING TURBULENCE MODELLING AND EXPERIMENTS 5, pp. 647-656, International Symposium on Engineering Turbulence Modelling and Measurements, Mallorca, Spain, 2002

A TEST CASE FOR LARGE-EDDY SIMULATION IN VEHICLE AERODYNAMICS

Siniša Krajnović[1] and Lars Davidson

Chalmers University of Technology,
Department of Thermo and Fluid Dynamics,
SE-412 96 Gothenburg, Sweden
http://www.tfd.chalmers.se/~lada/projects/sinisa/proright.html

ABSTRACT

Flow around a simplified bus was computed using large-eddy simulation (LES) with intention to gain better understanding of this flow and to make a data base for validation of Reynolds-averaged Navier-Stokes equations (RANS) and hybrid RANS-LES simulations. Transient quantities such as dominating frequencies and variance were studied as well as time-averaged quantities. Velocity and pressure results were compared with the experimental data. Coherent structures were visualized and their positions were determined. Time-averaged Reynolds stresses were computed and the largest resolved turbulent kinetic energy was found in the recirculating flow close to the leading edges and in the lower part of the wake.

KEYWORDS

Large-eddy simulation, LES, bluff body, vehicle aerodynamics, simplified bus

1 INTRODUCTION

Although large eddy simulation is not mature to be used for prediction of the flow around a passenger vehicle it can be used for prediction of the flow around car-like shapes at lower Reynolds number resulting in better understanding of this flow. Assuming that the Reynolds number is high enough to produce the flow similar to that around a full-scale vehicle, the obtained knowledge could

[1]E-mail: sinisa@tfd.chalmers.se

be used by the designer of the full-scale vehicle. The best known vehicle-like shape is Ahmed's body (Ahmed et al., 1984) which was studied both in experiments and numerical simulations (Han, 1989). A similar shape as Ahmed body is used in the experiments of Duell (1994) and Duell and George (1999). Krajnović and Davidson (2001a,b) made LES of this flow using insufficient near wall resolution and obtained the results in relatively good agreement with experiments. They found several difficulties when comparing their results with experimental data owing to the measurements technique used. The hot-wire anemometry resulted in a cooling velocity instead of three velocity components, and the pressure measurements were made only at the rear face of the model. This paper aims to present LES of this flow where the energy-rich near-wall coherent structures are resolved. Our simulation resulted in a data base which can be used by a vehicle designer. The data base is also useful for the CFD specialists for comparison with their RANS and hybrid RANS-LES simulations.

2 NUMERICAL METHOD

Calculations are made with the CALC-BFC code. This is based on an implicit a 3D finite volume method for solving the incompressible Navier-Stokes equations using a collocated grid arrangement. Both convective and viscous plus subgrid (SGS) fluxes are approximated by central differences of second order accuracy. A Crank-Nicolson second order scheme is used for time integration. The SIMPLEC algorithm is used for the pressure-velocity coupling. The code is parallelized using block decomposition and the PVM and MPI message passing systems (Nilsson and Davidson, 1998).

The effect of the small scales, which appears in the subgrid-scale stress tensor in the filtered Navier-Stokes equations, is modeled using the Smagorinsky model with the Smagorinsky constant C_s equal to 0.1. The formation of a turbulent boundary layer in the experiment was ensured with boundary layer trip wires mounted at the front of the model. Because of this there is no laminar boundary layer on the body and the assumption of non-zero SGS stresses used in our LES is thus correct.

3 DESCRIPTION OF THE TEST CASE AND NUMERICAL DETAILS

The computational domain and the bus model are presented in Fig. 1. All the geometric quantities are normalized with the body height H equal to 0.125m. A domain with an upstream length of $x_1/H = 8$, a downstream length of $x_2/H = 21$ and a spanwise width of $B = 5.92H$ was used for the simulation. Although the experimental studies (Duell, 1994; Duell and George, 1999) were carried out for several different aspect ratios (W/H), we chose $W/H = 1$, for which the drag and lift data exist from another experiment (Barlow et al., 1999b,a) using a similar body. The values of other geometrical quantities are $L/H = 3.68$, $S/H = 2.46$, $R/H = 0.152$, $r/H = 0.1016$ and $F/H = 4$. The ground clearance of $c/H = 0.08$ is similar to the clearance ratio of buses. The Reynolds number $Re = U_\infty H/\nu$ was 0.21×10^6.

In the experimental set-up, the location of the front side relative to the inlet was $4.512H$ and the distance from the test section exit to the back wall perpendicular to the flow was $14.832H$. A moving ground belt and boundary layer scoop were used to simulate the floor boundary condition and to minimize boundary layer effects. The cross-section of the tunnel test section, the ground clearance and the position of the model's cross-section with respect to the tunnel were identical in LES and the experimental set-up.

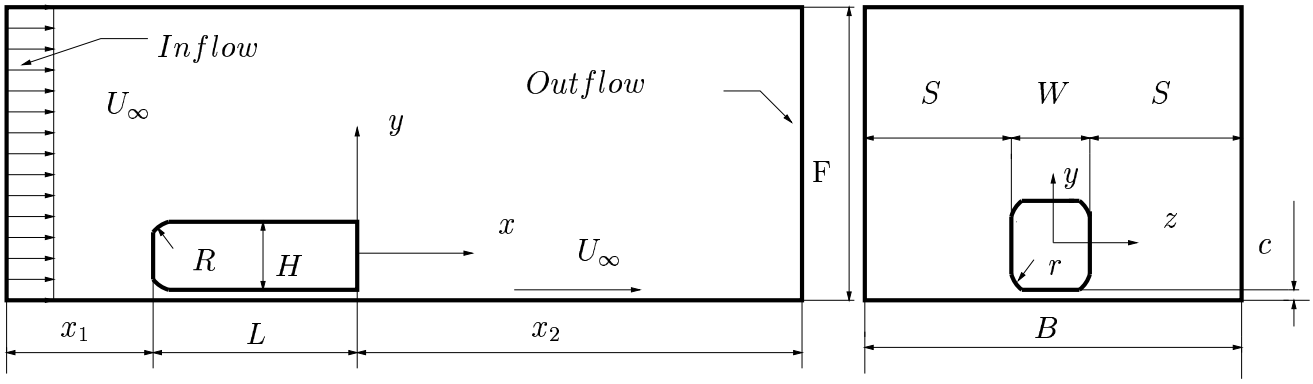

Figure 1: Geometry of the vehicle body and computational domain.

In the experiments of Duell and George (1994, 1999), the inlet mean velocity was uniform within 1% and the average turbulent intensity was 0.3%. A uniform velocity profile constant in time was thus used as the inlet boundary condition in this work. The convective boundary condition $\partial\bar{u}_i/\partial t + U_c\,(\partial\bar{u}_i/\partial x) = 0$ was used at the downstream boundary. Here, U_c was set equal to the incoming mean velocity, U_∞. To simulate the moving ground, the velocity of the lower wall was set equal to U_∞. The lateral surfaces were treated as slip surfaces using symmetry conditions $\partial\bar{u}/\partial z = \partial\bar{v}/\partial z = \bar{w} = 0$. No-slip boundary condition was used on the wall. The homogeneous Neumann condition was used for the pressure at all boundaries.

The topology of the computational grid consists of 40 blocks where 18 blocks form an O grid. An additional larger bus surface was made for the outer surface of the O grid. The O grid, with a thickness of $0.04H$, was created between this surface and the surface of the vehicle body. The total number of cells was 4.5 million resulting in the resolution on the top, bottom and lateral surfaces of the body expressed in the wall units $\langle\Delta s^+\rangle_t = 5-164$, $\langle\Delta n^+\rangle_t = 0.5-0.8$ and $\langle\Delta l^+\rangle_t = 14-142$. Here $\Delta f^+ = \Delta f u_\tau/\nu$, u_τ is the friction velocity and $\langle.\rangle_t$ denotes time averaging. s is the streamwise direction, n is the wall-normal direction and l is the direction parallel with the surface of the body and normal to the streamwise direction. This spatial resolution can be compared with the resolution in previous LES (Krajnović and Davidson, 2001a,b). These were characterized with $\langle\Delta s^+\rangle_t = 15-580$, $\langle\Delta n^+\rangle_t = 0.8-1.2$ and $\langle\Delta l^+\rangle_t = 14-217$ in the medium-grid simulation and $\langle\Delta s^+\rangle_t = 15-580$, $\langle\Delta n^+\rangle_t = 11.8-18.8$ and $\langle\Delta l^+\rangle_t = 14-217$ in the coarse-grid simulation. The time step was 1×10^{-4}, giving a maximal CFL number of approximately 6.5. The CFL number was smaller than one in 98% of the cells during the entire simulation. The averaging time in the simulation was $tU_\infty/H = 62.4$ (78000 time steps). The computational cost using 40 SGI R10000 CPUs was $\simeq$ 2300 hours (elapsed time).

4 RESULTS AND DISCUSSION

4.1 Time-averaged velocities

A series of time-averaged resolved velocities and turbulent stresses were computed. As mentioned earlier, only the mean cooling velocity $\overline{V}_{eff}$ defined as $\overline{V}_{eff} = \left(\overline{U}^2 + \overline{V}^2\right)^{1/2}$ where $\overline{U}$ and $\overline{V}$ are the mean velocity components in the x and y directions (see Fig. 1) is available from the experiments. For comparison with the experiments, $\overline{V}_{LES}$ was computed in LES as $\overline{V}_{LES} = \left(\langle\bar{u}\rangle_t{}^2 + \langle\bar{v}\rangle_t{}^2\right)^{1/2}$. Here, $\langle\bar{u}\rangle_t$ and $\langle\bar{v}\rangle_t$ are time-averaged resolved velocity components in the x and y directions, respectively, obtained from LES. The agreement of the velocity profiles from LES

with experiments is relatively good (see Fig. 2) but we found that the agreement of the present results with experiments is worse at $x/H = 0.32$ and $x/H = 0.98$ than the results presented in Krajnović and Davidson (2001a,b) where much coarser resolution was used (see Fig. 2). It is well known that the hot-wire anemometry technique used in experiments of Duell and George (1999) is not particularly accurate in the wake region (Bearman et al., 1989; Duell and George, 1999) where the flow is highly turbulent with regions of reversed flow. We computed the r.m.s. velocity intensity in the separation bubble and found that these were locally higher than 55% of the time-averaged velocity. Duell (1994) found that these intensities varied between 32% and 70%. According to Chandrsuda and Bradshaw (1981), the hot-wire measurements are reliable only if the r.m.s. velocity intensity is less than about 30%. Chandrsuda and Bradshaw (1981) also found that, when the turbulence intensity exceeds 50%, hot-wire results become highly unreliable. From this we conclude that the experimental data are not accurate in this region. Position $x/H = 1.63$ is downstream of the separation bubble, but the local turbulence intensity is still in excess by some 30% of the time-averaged velocity. The agreement of the LES profiles at this position with the experimental data becomes better with better spatial resolution (Fig. 2).

The free stagnation point (B_s) downstream of the separation bubble (Fig. 8a) is found to be below the center of the rear face of the bus with coordinates $x = 1.3H$ and $y = -0.2H$ (see Fig. 8a). Duell and George (1999) assumed the free stagnation point to be at $y = 0$, and measured the recirculation length $X_r = 1.1H$. Thus we computed the same length from our LES and found a value $X_r = 1.18H$ (Fig. 8a) close to the experimental one. We used both the local minimum of $\overline{V}_{LES}/U_\infty$ along the x-axis (used in the experiments of Duell and George (1999)) and change of sign in $\langle \bar{u} \rangle_t / U_\infty$ as indication of the closure of the separation bubble (see Fig. 3a).

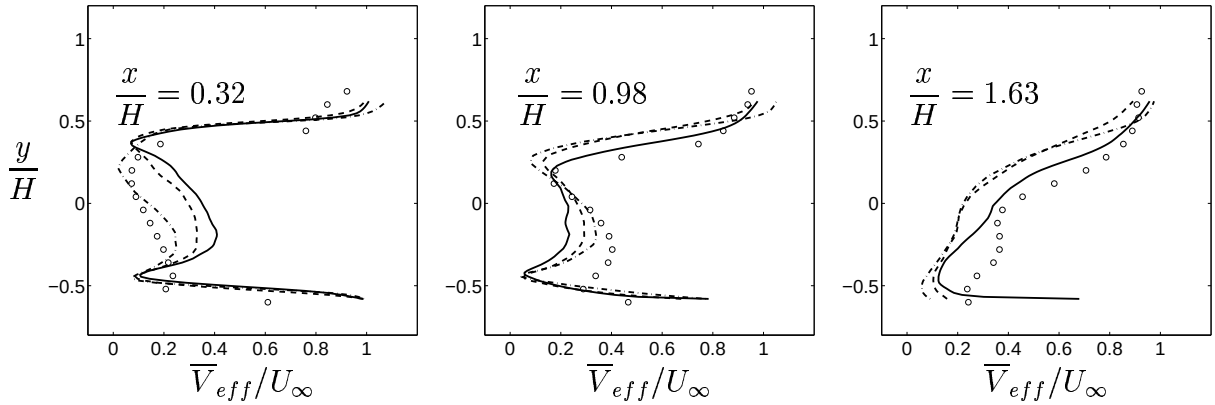

Figure 2: Time-averaged velocity profiles at three downstream locations at $z = 0$. Present fine-grid LES (solid line); previous medium-grid LES (Krajnović and Davidson, 2001b) (dashed line); previous coarse-grid LES (Krajnović and Davidson, 2001a,b) (dashed-dotted curve); experiment (symbols).

4.2 Surface pressure

The forces acting on the surface of the body as a result of the surface pressure were studied both time-averaged and instantaneously. The drag $\langle C_D \rangle_t$ and lift $\langle C_L \rangle_t$ coefficients that are interesting in engineering were computed to be 0.33 and -0.07, respectively, with variances $C_{D_{rms}} = 0.0075$ and $C_{L_{rms}} = 0.0033$. The drag and the lift coefficients measured in the experiments of Barlow et al. (1999b) for a similar body are 0.33 and -0.06, respectively. In addition to these quantities that are relevant for vehicle design, we studied the side force coefficient, C_S, and found that it varied with $C_{S_{rms}} = 0.0039$.

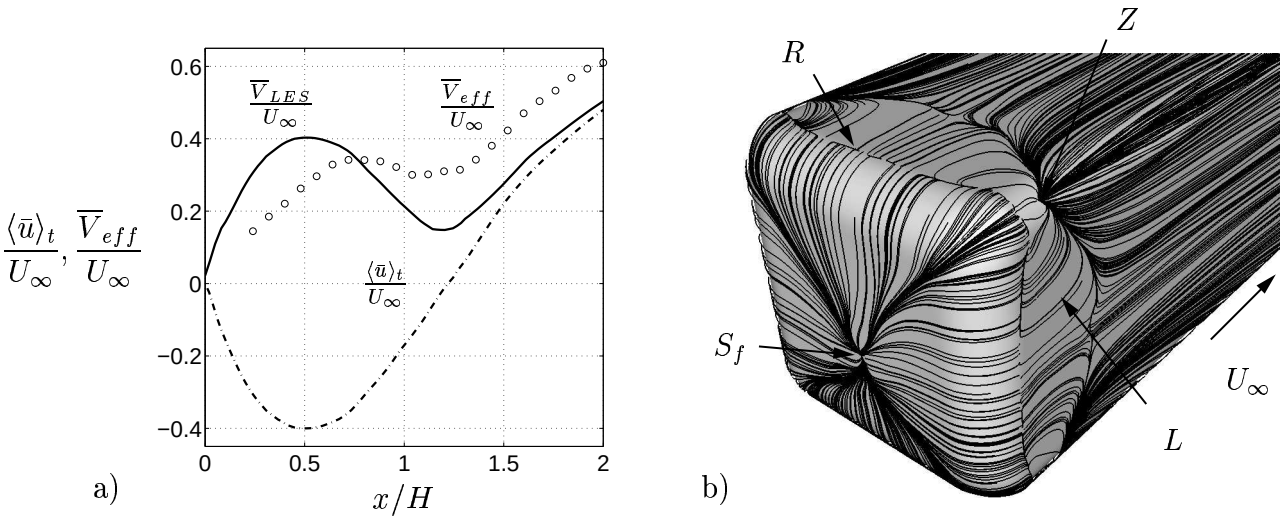

Figure 3: a) Distribution of the time-averaged velocity component $\langle\bar{u}\rangle_t/U_\infty$ and the time-averaged velocity $\overline{V}_{LES}/U_\infty$ compared with the experimental data ($\overline{V}_{eff}/U_\infty$) along the x-axis at $y = 0$, $z = 0$. b) Time-averaged trace lines on the surface of the body showing the roof vortex, R, the lateral vortex, L, and the stagnation point, S_f. View of the front face of the body.

The time history of these coefficients was studied and coefficient signals were Fourier transformed, resolving their dominating frequencies. Four dominating peaks were found in the Fourier transform of C_D at the Strouhal numbers $St = fH/U_\infty = 0.061, 0.14, 0.43$ and 0.73. The strongest peak was at $St = 0.061$, but the reliability of this frequency is weak owing to the short time history (averaging time correspond to approximately four periods of the signal). There were no peaks in the Fourier transform of C_L and two main frequencies at $St = 0.22$ and $St = 0.6$ were observed in the side-force signal. Thus we conclude that the motion of the wake in the spanwise direction is more rapid than in the floor-roof direction.

Unfortunately, only the pressure coefficient $C_p = (p - p_\infty)/(0.5\rho U_\infty^2)$ at the rear face of the body was measured in the experiments of Duell and George (1999). We computed the integrated value of C_p over the rear surface, $\langle\overline{C}_p\rangle_t$, to be -0.23 which is higher than the experimental value -0.286. This value is similar to the result in our previous LES and an explanation for the discrepancy between LES and experimental data is that, in our LES, we could not afford to resolve the boundary layer on the lateral walls of the channel, thereby reducing the blockage of the cross-section. A simple estimation of the displacement thickness at the position of the rear surface of the body gives a 5% decrease in the dynamic pressure, which is exactly the difference between our LES result and the experimental data. Also the $\overline{C}_p$ signal was Fourier transformed, revealing a dominating frequency of $St = 0.059$ which is close to the experimental value of 0.069 (note that this value was measured with static and not moving ground, see Duell and George (1999)).

4.3 Time-averaged coherent structures

The flow results in a number of vortices visualized in Figs. 3b - 9. As expected the flow separates on the rounded leading edges of the body and form two lateral vortices, L (one on each side of the body) and one vortex on the roof of the body, R. These vortices are visualized in Figs. 3b and 4 and the re-attachment lengths of the lateral vortices and the roof vortex, X_{R1} and X_S, respectively, (see Fig. 4) are $0.33H$. Following the flow along the body we observe two different kinds of streamwise vortices shown in Figs. 5 and 6, the upper-edge vortices (Fig. 5) (two on each

side of the body) and the lower-edge trailing vortices T (Fig. 6) (one on each side of the body). Vortices U_p and U_s (Fig. 5) are formed in the point Z (Fig. 3b) and are located on the rounded top-side edge of the body (Fig. 5). The inclination of the trace lines around the rounded side edge in Fig. 3b shows the location of these vortices along the body. These vortices are present along the entire bus.

The flow under the body is only partly transported to the rear edge of the body and a substantial amount of fluid flows to the lateral sides and form the trailing vortices T. These vortices are present from the re-attachment of the lateral vortices L (Fig. 3b), at $x = -3.36H$ to approximately $x = 0.4H$. On their way downstream the T vortices first grow in diameter, reaching their maximum in the vicinity of the rear face of the body ($x = 0$), and then shrink further downstream (Fig. 6). Although they form at the surface near the re-attachment line, they move away from the body in the lateral direction and towards the channel floor as they pass the body (Fig. 6). None of the trailing vortices that were found in the time-averaged flow (Figs. 5 and 6) are present in the instantaneous flow (Fig. 7). The time-averaged vortices are in the instantaneous flow replaced with coherent structures that move randomly in time and space (Fig. 7).

The boundary-layer grows along the body surface and finally separates at the sharp rear edges of the body and forms two counter-rotating vortices in the $x - y$ plane with foci F1 and F2 in Fig. 8a. Figure 8a shows that the upper vortex the plane $z = 0$ is much larger that the lower one owing to the small ground clearance which suppresses the flow entering the wake from under the body. Similar pair of vortices is formed in the $x - z$ plane and these together with the vortices in the $x - y$ plane form the vortex ring, W, shown in Fig. 8b. One additional group of thin vortices (B in Fig. 8) is formed close to the sharp rear edges caused by the abrupt separation of the flow. The cores of ring vortex W, edge vortices B, and trailing vortex T are visualized in this figure using the critical-point theory (Chong et al., 1990; Sujudi and Haimes, 1995), i.e. we plotted the points whose rate-of-deformation tensor has one real and a pair of complex-conjugate eigenvalues and whose velocity is zero.

After the closure of the separation bubble in Figs. 8 and 9a, a pair of counter-rotating longitudinal vortices is formed. The direction of the rotation of these vortices is such that the fluid in the space between them is transported towards the floor. They move towards the floor and against each other with increasing distance from the bus. Close to the floor they deflect sideways away from the symmetry plane $z = 0$. They were detected as far as at the outlet ($x/H = 21$) showing the adequacy of such a long downstream length of the computational domain and the convective outlet boundary condition. Also these time-averaged vortices are the result of a number of instantaneous vortices which move in space and time (Fig. 9b).

4.4 Reynolds stresses

In addition to time-averaged velocities and pressure, resolved Reynolds stresses were also computed and studied. One isosurface of high magnitude of resolved turbulent kinetic energy $\langle k \rangle_t = 1/2 \langle u_i' u_i' \rangle_t$ can be seen in Fig. 10a. It was found that the regions of the highest turbulence intensity are the roof vortex, R, and the lateral vortices, L (Fig. 10a). The reason why $\langle k \rangle_t$ is large here is because the separation bubbles are highly unsteady, with an almost periodic behavior. The lower vortex in the wake (Fig. 8a) was found to be more turbulent than the upper one and this is because the fluid entering the wake from under the body is more unsteady than the fluid entering the upper vortex. High levels of $|\langle v'w' \rangle_t|$ occur along the upper-edge vortices U_p and U_s and the lower-edge vortices T (Fig. 10b).

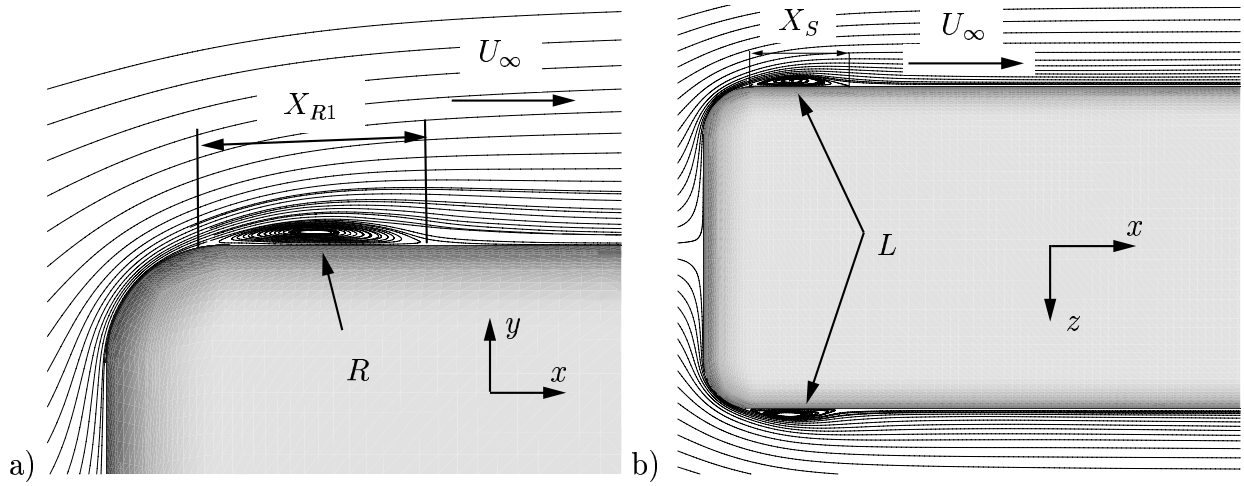

Figure 4: a) Time-averaged streamlines projected onto plane $z = 0$. The direction of the rotation of R is clockwise. b) Time-averaged streamlines projected onto plane $y = 0$. The direction of the rotation of vortices L is clockwise for $z < 0$ and counter-clockwise for $z > 0$.

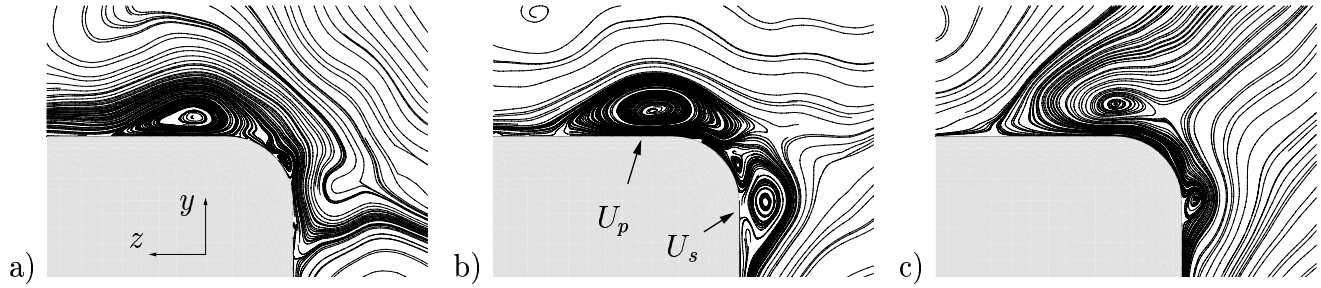

Figure 5: Time-averaged streamlines projected onto planes: a) $x = -2.08H$, b) $x = -1.28H$ and c) $x = -0.48H$. The direction of the rotation of vortices U_p and U_s is counter-clockwise and clockwise respectively. View from behind of the upper-right edge of the body.

5 CONCLUDING REMARKS

Large-eddy simulation can provide large amount of data for the flow around vehicle-like bluff bodies. This data can be used as a tool for understanding the flow around such bodies and for tuning turbulence models. If the simulation is properly performed the near-wall flow can be well represented and this data can be used for validation of near-wall modeling in future LES or hybrid LES-RANS simulations.

Although the geometry of the body studied in this paper is relatively simple the flow around it appears to be very complex. Our LES was successful to predict not only the separation regions close to the leading edge of the body and the vortex ring in the wake but also the trailing vortices and the very thin vortices close to the rear edge of the body.

Engineers relay mostly on the time-averaged quantities of the flow but instantaneous flow can also be important. Therefore we studied the time history of the flow presented in this paper and computed dominating frequencies of the pressure forces acting on the body.

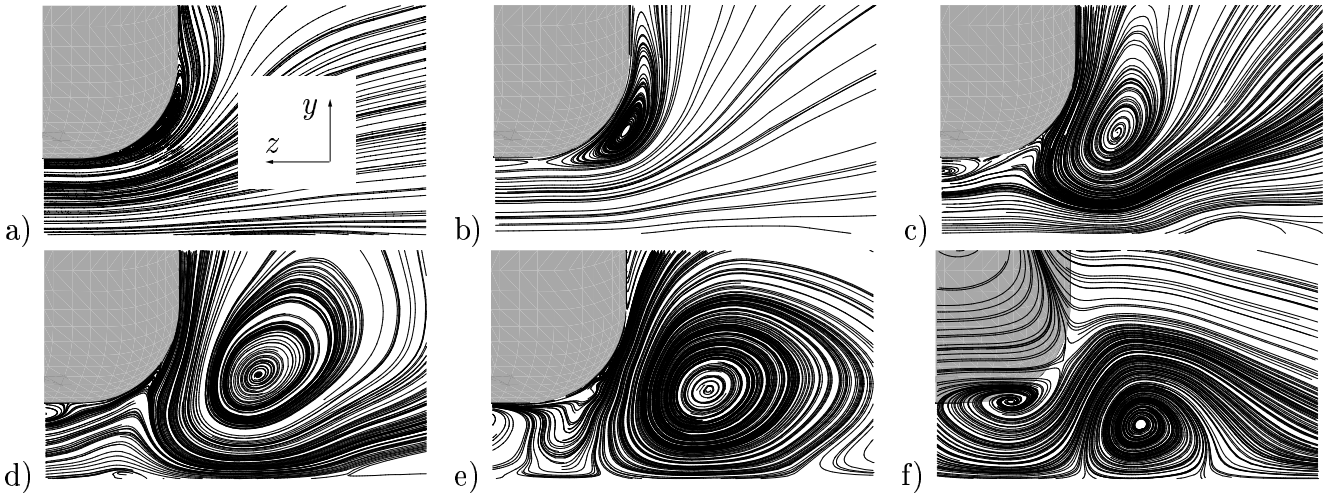

Figure 6: Time-averaged streamlines projected onto planes: a) $x = -3.36H$, b) $x = -2.88H$, c) $x = -1.68H$, d) $x = -0.48H$, e) $x = 0$ and f) $x = 0.32H$. The direction of the rotation of this vortex is counter-clockwise. View from behind of the lower-right edge of the body.

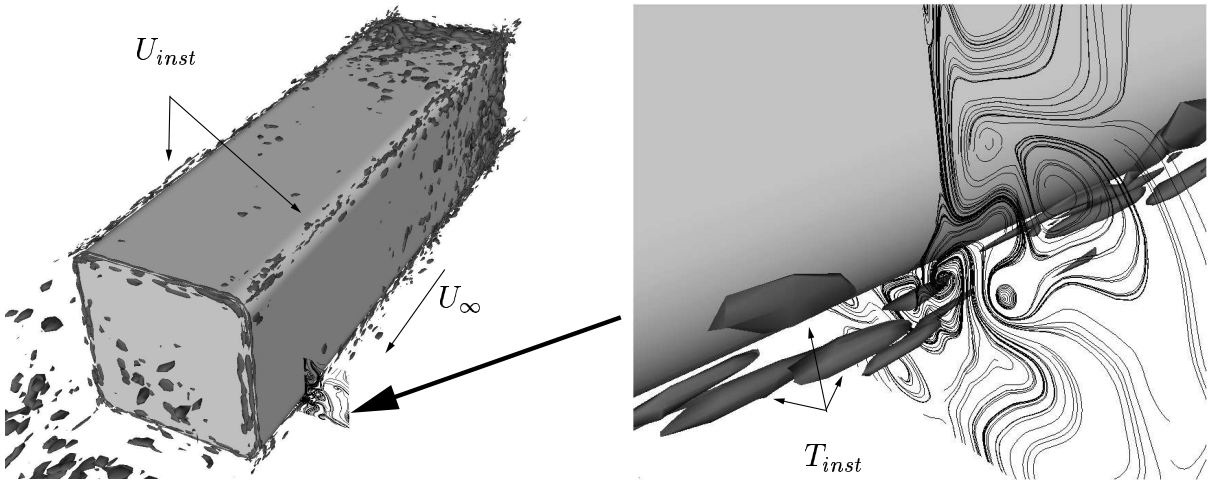

Figure 7: The isosurface of the instantaneous second invariant of the velocity gradient (see Jeong and Hussain (1995)) $Q = 13500$ and the streamlines in plane $x = -0.48H$. U_{inst} and T_{inst} are the instantaneous coherent structures close to the upper and the lower edges respectively. Left: view of the rear face of the body; right: zoom.

6 ACKNOWLEDGMENTS

This work was supported by NUTEK and Volvo Car Corporation. Computer time on the SGI ORIGIN 2000 machines, provided by UNICC at Chalmers, is gratefully acknowledged.

REFERENCES

Ahmed, S. R., Ramm, G., Faltin, G. (1984). Some salient features of the time averaged ground vehicle wake. SAE Paper 840300.

Barlow, J., Guterres, R., Ranzenbach, R., Williams, J. (1999a). Wake structures of rectangular bodies with radiused edges near a plane surface. SAE Paper 1999-01-0648.

Barlow, J. B., Guterres, R., Ranzenbach, R. (1999b). Rectangular bodies with radiused edges in

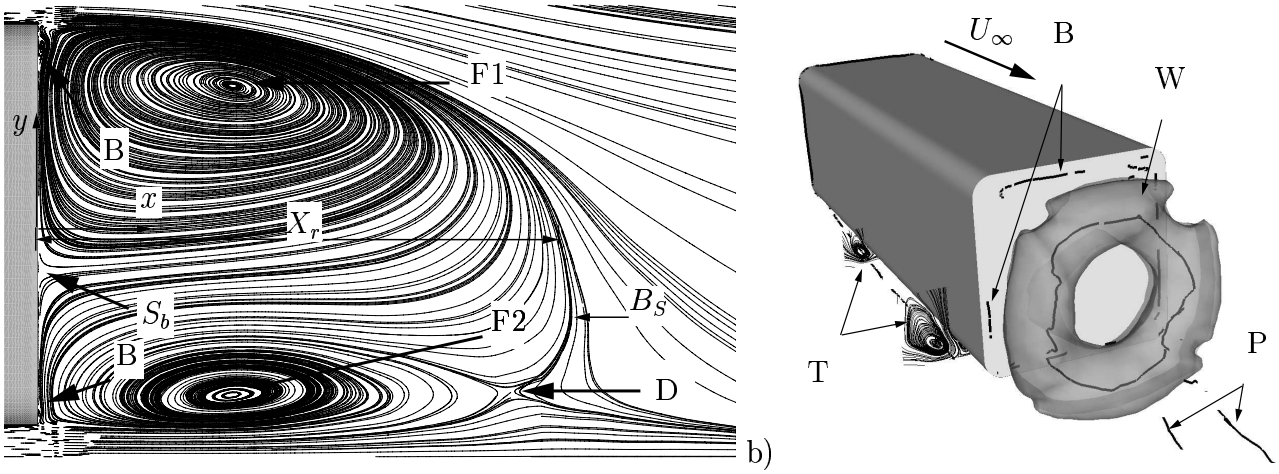

Figure 8: a) Time-averaged streamlines projected onto symmetry plane $z = 0$ of the bus. S_b is the stagnation point on the rear face of the bus, B_S is the free stagnation point and D is the saddle point. b) The isosurface of the time-averaged pressure $p = -0.20$. The black curves represent the vortex cores of thin edge vortices B, ring vortex W and longitudinal vortices P behind the separation bubble. Vortex on the left side ($z > 0$) T is visualized using streamlines in planes $x = -2.08$ and $x = -0.48H$, respectively. View of the rear face of the body.

ground effect. AIAA paper 99-3153.

Bearman, P. W., Beer, D. D., Hamidy, E., Harvey, J. K. (1989). The effect of a moving floor on wind-tunnel simulation of road vehicles. SAE Paper No. 880245.

Chandrsuda, C., Bradshaw, P. (1981). Turbulence structures of reattaching mixing layer. Journal of Fluid Mechanics 110, 171–194.

Chong, M. S., Perry, A. E., Cantwell, B. J. (1990). A general classification of three-dimensional flow fields. Physics of Fluids 5 (2), 765–777.

Duell, E. G. (1994). Experimental investigation of unsteady near wakes of ground vehicle bodies. Ph.D. thesis, Cornell University.

Duell, E. G., George, A. R. (1999). Experimental study of a ground vehicle body unsteady near wake. SAE Paper 1999-01-0812.

Han, T. (1989). Computational analysis of three-dimensional turbulent flow around a bluff body in ground proximity. AIAA Journal 27 (9), 1213–1219.

Jeong, J., Hussain, F. (1995). On the identification of a vortex. Journal of Fluid Mechanics 285, 69–94.

Krajnović, S., Davidson, L. (2001a). Large eddy simulation of the flow around a ground vehicle body. In: SAE 2001 World Congress. SAE Paper 2001-01-0702, Detroit, Michigan, USA.

Krajnović, S., Davidson, L. (2001b). Large eddy simulations of the flow around a simplified bus. In: Liu, C., Sakell, L., Beutner, T. (Eds.), 3rd AFOSR International Conference on DNS and LES. Greyden Press, Arlington, Texas, pp. 775–782.

Nilsson, H., Davidson, L. (1998). CALC-PVM: A parallel SIMPLEC multiblock solver for turbulent flow in complex domains. Int.rep. 98/12, Dept. of Thermo and Fluid Dynamics, Chalmers University of Technology, Gothenburg.

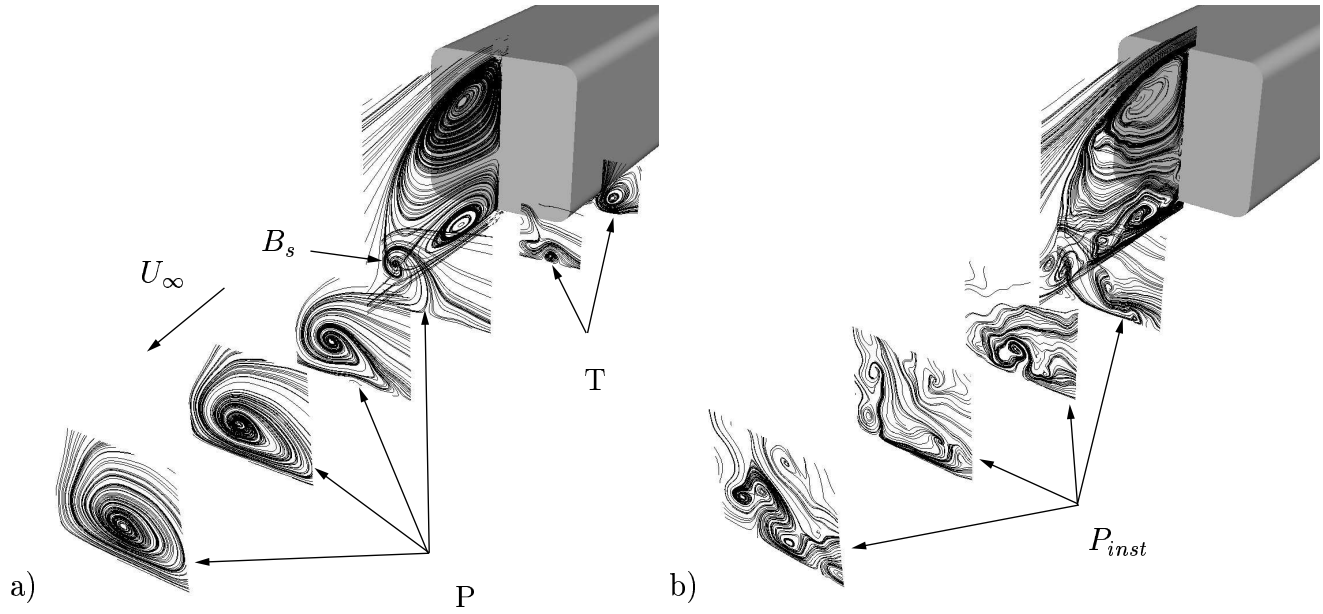

Figure 9: Streamlines in the time-averaged flow in figure a) and in the instantaneous flow in figure b). Time-averaged (P) and instantaneous (P_{inst}) longitudinal vortices are visualized in both figures in planes $x/H = 1.36$, $x/H = 2.16$, $x/H = 2.96$ and $x/H = 3.76$. Time-averaged trailing vortex T is shown in figure a) in planes $x/H = -0.48$ and $x/H = 0.4$ (note that only the longitudinal vortices for $z < 0$ are shown in this figure). The direction of the rotation of the right ($z < 0$) time-averaged vortices P and T is counter-clockwise. View of the rear face of the body.

Sujudi, D., Haimes, R. (1995). Identification of swirling flow in 3-D vector fields. AIAA Paper AIAA 95-1715.

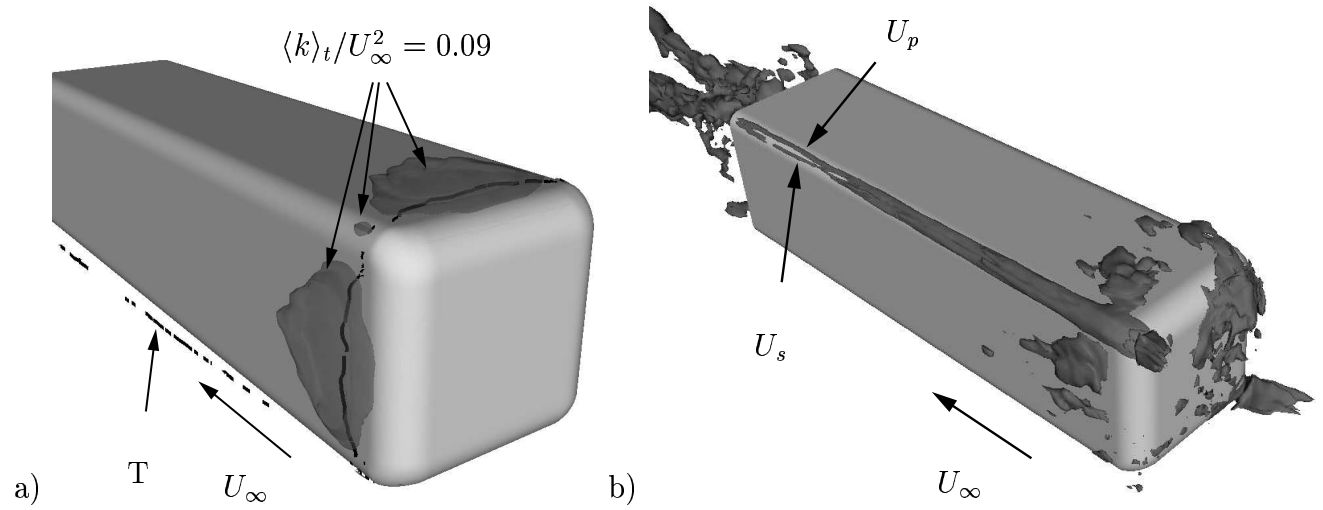

Figure 10: a) The isosurface of the resolved turbulent kinetic energy $\langle k \rangle_t / U_\infty^2 = 0.09$. The black curves indicates the positions of the vortex cores of the roof vortex, lateral vortices and the lower-edge vortex T. b) The isosurface of the $\langle v'w' \rangle_t / U_\infty^2 = 2.3 \times 10^{-4}$. View of the front face of the body.